Article:
Niu, C., Chen, B., Fletcher, S. et al. (2026) Learning-based robotic machining error prediction for high precision manufacturing. Robotics and Computer-Integrated Manufacturing, 100. 103217. ISSN: 0736-5845

https://doi.org/10.1016/j.rcim.2025.103217

Highlights

Learning-Based Robotic Machining Error Prediction for High Precision Manufacturing

Chaoyue Niu, Bin Chen, Simon Fletcher, Peace Onawumi, Erdem Ozturk, Mahdi Mahfouf, Visakan Kadirkamanathan

- Novel solution predicts machining errors without costly CMM inspection.
- Identifies optimal sensor–controller data combination for error prediction.
- Best model achieves seven improvements over raw laser sensor-based error prediction.
- Models validated to match CMM accuracy across three scenarios.

Learning-Based Robotic Machining Error Prediction for High Precision Manufacturing

Chaoyue Niu[a,*], Bin Chen[a], Simon Fletcher[b], Peace Onawumi[c], Erdem Ozturk[c], Mahdi Mahfouf[a] and Visakan Kadirkamanathan[a]

[a]School of Electrical and Electronic Engineering, University of Sheffield, Sheffield, S10 2TN, U.K.
[b]School of Computing and Engineering, University of Huddersfield, Huddersfield, HD1 3DH, U.K.
[c]Advanced Manufacturing Research Centre, University of Sheffield, Rotherham S60 5TZ, U.K.

ARTICLE INFO

Keywords:
Robot Manufacturing
Data-Driven Modelling
Machining Error Prediction
Laser Tracker
Machine Learning

ABSTRACT

High precision machining with robots is an open challenge. Achieving precision of dimensional and geometrical features with robotic machining would require compensation via feedback control which relies on accurate error prediction. Machining error prediction is a complex problem in high-precision manufacturing, where effective solutions must accurately estimate geometrical errors in different workpieces while minimizing quality inspection costs. It is also compounded by the need for real-time estimation for feedback control. This paper introduces a novel approach for predicting the quality of milled workpieces using low-cost, in-process signals and machine learning. The proposed method fuses internal machine controller commands—comprising end-effector trajectory coordinates and angular changes of six revolute joints in the robotic arm—with external laser tracker sensing signals that capture the real trajectory of the milling tool and predicts dimensional errors as would be obtained by a Coordinate Measuring Machine (CMM). To overcome the lack of knowledge of the dependence of the part dimensional error on the available signals, models with varying combinations of the sensors and the length of the time window of historical data for inclusion in the model were evaluated. In addition, five machine learning algorithms were selected, trained, evaluated and validated on data from two distinct workpieces and various spatial configurations. The best machine learning model achieved a sevenfold improvement in dimensional error prediction compared to solely using laser tracker data, with mean absolute error reduced from 0.0756 mm to 0.0097 mm. This study demonstrates the feasibility of using low-cost, in-process sensing signals to predict high-precision quality dimensional data that is normally measured by costly CMMs, enabling rapid part quality inspection and significant potential cost reduction.

1. Introduction

Global manufacturing is being transformed by disruptive technologies, pushing towards autonomous production and digitized value chains [1]. Future factories will need to be faster, more agile, and closer to customers, enabling mass customization of affordable, on-demand products [2]. Metrology is crucial in this context for ensuring quality and improving productivity. Metrology data analytics [3] is set to revolutionize manufacturing by creating a unified metrology knowledge system that standardizes data usage across design, production, and verification stages. Robotic systems, traditionally used in low-force, low-precision tasks, are now being explored for high-force, high-precision processes such as milling [4]. Integrating advanced metrology analytics [5] with robotics can overcome control challenges, enabling real-time error prediction and process optimization to meet stringent quality standards of high precision manufacturing.

In conventional manufacturing, part quality is typically assessed post-process using high-accuracy inspection methods such as Coordinate Measuring Machines (CMMs) [6]. While CMMs offer exceptional precision in measuring geometric features, they are costly, time-intensive, and require transferring the part from the production line to an inspection station, resulting in operational inefficiencies. Furthermore, CMMs operate offline, providing no real-time feedback during machining, which complicates the detection and rectification of errors as they occur. Alternative

*Corresponding author
c.niu@sheffield.ac.uk (C. Niu); bin.chen@sheffield.ac.uk (B. Chen); s.fletcher@hud.ac.uk (S. Fletcher); peace.onawumi@ntu.ac.uk (P. Onawumi); e.ozturk@sheffield.ac.uk (E. Ozturk); m.mahfouf@sheffield.ac.uk (M. Mahfouf); visakan@sheffield.ac.uk (V. Kadirkamanathan)
ORCID(s): 0000-0001-7626-0317 (C. Niu)

inspection methods, such as optical systems [7], offer rapid and non-contact measurement capabilities; however, they are often hindered by challenges in handling reflective surfaces, complex geometries, and fine tolerances, making them less suitable for high-precision milling. Likewise, touch probes [8] provide precise, contact-based measurements but are inherently slow and disruptive, as they require halting the process for inspection, thereby impeding real-time corrections. The constraints of these conventional methods underscore a critical need for novel, real-time, and cost-effective metrology solutions for robotic machining.

Extensive research has investigated robot error modeling and on-machine measurement for high-precision manufacturing. Early studies focused on geometric error compensation of machine tools and industrial robots using laser trackers, theodolites, or vision systems to improve absolute positioning accuracy [9, 10, 11, 12, 13]. Theoretical approaches model kinematic and pre-travel errors based on rigid-body or dynamic models of the robot and probe [14, 15, 16, 17], while experimental and calibration-based methods employ extensive offline measurements to generate error maps [18]. Additionally, research on robotic precision and path tracking has made significant progress through position-based visual servoing (PBVS) and iterative learning control (ILC) strategies. For example, switch-based sliding mode control has shown strong robustness in robotic riveting, effectively compensating for model uncertainties and external disturbances during path following and spot positioning [19], and calibration-based ILC has improved path tracking accuracy by iteratively identifying and correcting robot kinematic parameters [20]. Despite their effectiveness, these control-oriented methods face several limitations when applied to high-precision robotic machining. They rely heavily on accurate kinematic and dynamic models, which are difficult to obtain or maintain under changing tool–workpiece conditions. They often require costly visual or geometric calibration setups. Moreover, while they improve motion and trajectory accuracy, they do not directly predict or quantify machining errors, which are critical for precision assurance and real-time quality feedback. Consequently, a critical gap remains in developing methods capable of learning the mapping between in-process sensing signals and part quality.

Data-driven models leveraging machine learning trained on low cost in-process sensor data offers a promising approach to address the challenge of machining error prediction. Industry 4.0 has spurred machine learning advancements for error prediction [21], including wavelet-enhanced CNNs for fault diagnosis [22], learning methods for quality prediction [23], and CNN-LSTM models for surface roughness in milling [24]. In-process error compensation methods [25] and probabilistic frameworks [26] have been explored but only for robot drilling where error prediction for the depth of cut can be achieved relatively easily. A core challenge of developing robust techniques for in-process quality monitoring and prediction without relying on expensive and time-consuming offline measurement methods for high precision machining still exists.

Laser trackers [27] and advanced computer numerically control (CNC) controllers [28] represent promising alternatives for enhancing real-time quality prediction in robotic systems. Laser trackers offer a relatively low-cost yet high-precision solution for tracking the real-time position and trajectory of a robot's end-effector. This can be correlated with the part's shape and geometries to some extent. However, a direct correlation between the laser tracker data and part quality is often hindered by factors such as the tool's interaction dynamics with the workpiece [29], environmental influences (e.g., temperature fluctuations [30], humidity [31], air pressure [32], mechanical strain [33] and surface contamination [34]), and the limitations in tracking accuracy that may not fully capture the complexities of machining processes. This means that the direct laser tracker measurement cannot provide a highly accurate dimensional measures necessary for quality inspection. Siemens controllers provide detailed spatial information about the milling process, including machine dynamics, position, and angular changes of robotic joints. This contextual information can serve as a potential source for understanding tool movement and part geometries. The integration of contextual data from CNC controllers with that of laser trackers offers a promising approach to real-time quality inspection. By combining the precise positional data from laser trackers with the detailed machine dynamics and spatial information from CNC controllers, a unified model could be developed to enhance predictive accuracy. Effective integration of these technologies could provide a robust solution for real-time quality assessment, advancing the capabilities of robotic systems in high-precision manufacturing processes.

This paper builds on the idea of combining laser tracker and Siemens controller information and proposes a data-driven approach to predict part quality during robotic milling. Specifically, we develop a robust data-driven model that incorporates key variables such as the discrepancy between the laser tracker and controller positional data (ϵ_{Laser}), the CMM-nominal size error (ϵ_{CMM}), angular variations of the robot's six revolute joints. These features are processed in real time to predict machining errorsduring high-force milling operations. The model is built on the foundation of machine learning techniques, namely, Random Forest, Decision Tree, Gradient Boosting, K-Nearest Neighbors and Multilayer Perceptron Neural Networks.

The novelty of the developed method lies in leveraging in-process sensing to predict dimensional and geometrical errors, rather than relying solely on offline inspection. This approach enables the continuous estimation of part quality during machining, providing timely feedback that can inform subsequent control or adjustment actions. Compared to traditional offline inspection, which evaluates errors only after the part is fully machined, in-process prediction offers the potential to identify deviations earlier in the manufacturing process, reducing the risk of producing defective parts and enhancing overall process efficiency when combined with the concept of *inspection by exception* [25, 35]. This method provides a more dynamic and responsive framework for quality monitoring, bridging the gap between conventional error modelling and real-time error awareness in high-precision robotic machining.

This paper contributes to the field of robotic milling and part quality prediction in four key ways. First, it presents a novel data-driven model that integrates low-cost, in-process sensor data from laser trackers and Siemens controllers to predict part dimensional error, that is traditionally measured using a coordinate measuring machine (CMM). Second, by noting the raw laser sensor data did not correlate with goal standard CMM error values, identification of the optimal combination of sensor and controller data for error prediction was made. Third, it builds a range of machine learning algorithms—including Decision Tree [36], Neural Network [37], Gradient Boosting [38], Random Forest [39] and K-Nearest Neighbors (KNN) [40]—for accurate dimensional error prediction, accounting for temporal dependencies and diverse feature set combinations. Fourth, the effectiveness of the proposed model is validated through a comprehensive analysis involving two distinct workpieces, with square and circular features in terms of dimensional error prediction.

The remainder of this paper is organized as follows: Section 2 details the data collection methodology with field trials on a robotic arm to mill square and circular parts while capturing in-process sensing signals. It also formulates the research problem and introduces the selected data-driven models. In Section 3, five machine learning algorithms are implemented, and identifies the most effective models through the assessment of their performance based on model complexity, aggregated model prediction error measures, and mean machining error prediction accuracy. Section 4 revisits the research problems, confirming their validity, and provides a critical analysis of the findings, addressing potential limitations and uncertainties while suggesting future research directions. Finally, Section 5 synthesizes the key insights and contributions of the study.

2. Materials and Methods

2.1. Problem formulation

The problem arises from the challenge of whether the observed deviations in CMM measurements, which capture the ground truth of machined workpiece geometries, can be modelled and predicted accurately using information derived from laser trackers. This results in two main problems, with the first relating to how the laser tracker data based prediction generalises and the second being related to if additional data needs to be included for improved prediction.

2.1.1. Predicting CMM Data from Laser Tracker Data

The first problem is formulated as determining whether the CMM data can be predicted using only laser tracker data, and how well this approach generalizes across different workpieces and layers. This can be mathematically described as,

$$\epsilon_{\mathrm{CMM},\mathcal{W}} = f\left(\epsilon_{\mathrm{Laser},\mathcal{W}}\right) + \varepsilon \tag{1}$$

where $\epsilon_{\mathrm{CMM},\mathcal{W}}$ and $\epsilon_{\mathrm{Laser},\mathcal{W}}$ represent the deviations measured by the CMM and laser tracker, respectively, for workpiece $\mathcal{W}$, and ε is the modelling error term. Testing the generalisation of how well this relationship has been learned can be broken down into three specific scenarios:

The first scenario involves predicting CMM data on different workpieces, not just on the same one. Let $\mathcal{W}_1$ and $\mathcal{W}_2$ represent two distinct workpieces, and consider layer l in both. The task is to train a model using the deviation between laser tracker data and Siemens controller data, $\epsilon_{\mathrm{Laser},\mathcal{W}_1,l}$, from workpiece $\mathcal{W}_1$ and predict the corresponding deviation between CMM measurements and nominal dimensions, $\epsilon_{\mathrm{CMM},\mathcal{W}_2,l}$, for the same layer l in workpiece $\mathcal{W}_2$. The model learning is mathematically formulated as:

$$\epsilon_{\mathrm{CMM},\mathcal{W}_1,l} = f_{1,l}\left(\epsilon_{\mathrm{Laser},\mathcal{W}_1,l}\right) + \varepsilon_{1,l} \tag{2}$$

and the prediction

$$\hat{\epsilon}_{\text{CMM},\mathcal{W}_2,l} = f_{1,l}\left(\epsilon_{\text{Laser},\mathcal{W}_2,l}\right) \tag{3}$$

where $f_{1,l}(\cdot)$ denotes the predictive model learned from the work piece $\mathcal{W}_1$ data. The goal is to achieve a low prediction error, which would indicate that the model generalizes well to different workpieces for the same layer.

The second scenario involves predicting CMM data for different layers in different workpieces, rather than using the same layer for different workpieces. Now consider layers l_1 and l_2 in workpieces $\mathcal{W}_1$ and $\mathcal{W}_2$, respectively, where $l_1 \neq l_2$. The objective is to train a model on $\epsilon_{\text{Laser},\mathcal{W}_1,l_1}$ and predict the CMM data $\epsilon_{\text{CMM},\mathcal{W}_2,l_2}$ for a different layer. Mathematically:

$$\hat{\epsilon}_{\text{CMM},\mathcal{W}_2,l_2} = f_{1,l_1}\left(\epsilon_{\text{Laser},\mathcal{W}_1,l_1}\right) \tag{4}$$

This problem is more challenging due to variations in geometric and dynamic properties across different layers of the machining processes, impacting model accuracy.

The third scenario involves predicting CMM data by reversing the modelling order on different workpieces, testing whether the prediction performance remains consistent regardless of the order of modelling. An additional complexity arises when we reverse the training and testing workpieces, i.e., training on $\mathcal{W}_2$ and testing on $\mathcal{W}_1$. This task can be described as evaluating

$$\hat{\epsilon}_{\text{CMM},\mathcal{W}_1,l} = f_{2,l}\left(\epsilon_{\text{Laser},\mathcal{W}_1,l}\right) \tag{5}$$

and testing if the prediction errors arising from the functions $f_{1,l}(\cdot)$ and $f_{2,l}(\cdot)$ are similar.

These three strategies will evaluate model robustness across different parts, ensuring generalizability to new, unseen data.

2.1.2. Identifying Key Features for CMM Modeling

While the laser tracker captures the movement of the end-effector, it may not fully explain the deviations in CMM data against nominal size. Integrating robot X and Y coordinates is crucial for accurate CMM prediction, as the robot's behaviour changes with position and feed rate. Laser data captures effects but not the underlying causes, while position data helps model these dynamics for more accurate predictions (see Figure 3B and D). The second problem is to identify additional features that significantly influence the prediction of CMM data. We investigate the impact of incorporating spatial information of milling tool/end effector and angular changes of six revolute joints of the robotic system, leading to three distinct scenarios:

Incorporating Spatial Information (X and Y Coordinates) Let $X_{\mathcal{W},l}$ and $Y_{\mathcal{W},l}$ denote the spatial X and Y coordinates of the end-effector for a given workpiece $\mathcal{W}$ and layer l.

Incorporating Angular Changes of the Robotic Joints $\Delta\theta$ The robot arm's six joint angular changes $\Delta\boldsymbol{\theta}_{\mathcal{W},l} = [\Delta\theta_1, \Delta\theta_2, \ldots, \Delta\theta_6]$, affect both the end-effector dynamics and the induced machine deformations.

Combining Spatial and Angular Features The most comprehensive model incorporates laser, spatial and angular features:

$$\epsilon_{\text{CMM},\mathcal{W},l} = \begin{cases} g(\epsilon_{\text{Laser},\mathcal{W},l}, X_{\mathcal{W},l}, Y_{\mathcal{W},l}) + \varepsilon, & \text{(spatial features)} \\ h(\epsilon_{\text{Laser},\mathcal{W},l}, \Delta\boldsymbol{\theta}_{\mathcal{W},l}) + \varepsilon, & \text{(joint angle features)} \\ q(\epsilon_{\text{Laser},\mathcal{W},l}, X_{\mathcal{W},l}, Y_{\mathcal{W},l}, \Delta\boldsymbol{\theta}_{\mathcal{W},l}) + \varepsilon, & \text{(spatial + joint angle features)} \end{cases} \tag{6}$$

where $g(\cdot)$, $h(\cdot)$, and $q(\cdot)$ are the functions being modelled and ε represents the modelling error.

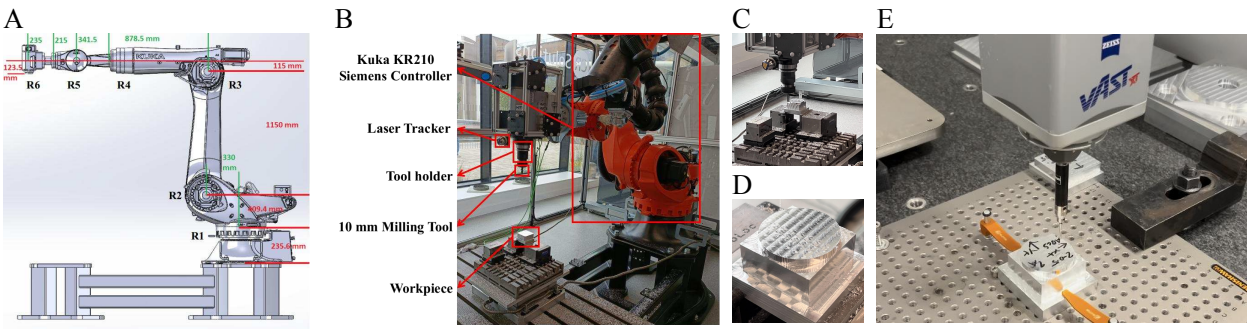

Figure 1: The robot platform setup and quality measurement for data collection. **A**. KUKA KR210 robot dimension. R1 - R6 denote the six revolute joints of the robotic system. **B**. Sensor and workpiece setup. **C**. Milling process. **D**. A roughing milled part that is geometrized by a bottom square with a nominal dimension of 48.2 mm and a top circle with a nominal diameter of 47.4 mm. **E**. Coordinate measuring machine that measures the part quality with a 1mm diameter probe.

While Eq. 6 with spatial features includes only the X and Y coordinates of the tool tip, it implicitly incorporates information about the full tool pose, including both position and orientation, through the deviation between the laser tracker measurements and the Siemens controller data. Factors such as tool radius, tool deflection, and milling forces also influence machining errors. In this study, their effects are partially captured by the laser tracker measurements, as any displacement of the tool tip resulting from deflection or cutting forces is inherently recorded. Furthermore, our investigation focused on a typical machining metrology setup using a laser tracker, which constrained the available dataset to the measurements used in this work.

The joint displacement values used in this study correspond to the actual measured values. The dynamic behavior of the robot, including vibrations and compliance in different configurations, can affect machining accuracy. In our approach, these dynamic effects are implicitly captured by the deviations between the laser tracker measurements and the Siemens controller commands. Although robot dynamics are not explicitly modeled, the measured deviations effectively reflect their overall impact on machining errors.

The overarching goal is to identify the optimal feature set that can accurately predict CMM deviations under various scenarios and workpiece conditions. By systematically analyzing different combinations of features, we can also derive insights into the primary drivers of CMM deviations, aiding a better understanding and modelling the manufacturing process.

2.2. Data collection

The experimental data is collected utilising a standard KUKA KR210, a 6-axis industrial robot. The robot was equipped with an end-effector featuring a milling tool with a diameter of 10 mm, and its operations were controlled by a Siemens 840D solution line controller, while the position data was recorded via OPC UA at a sampling frequency of 10 Hz. To accurately track the real-time movement of the milling tool, a laser tracker (Leica Absolute Tracker ATS600) was employed, operating at a higher frequency of 100 Hz, for precise monitoring of the tool's dynamic behaviour. The robot dimensions and experiment configuration are shown in Figures 1A and 1B. Figures 1C and 1D illustrate the milling process and the resulting milled component, which features square and circular geometries. Figures 1E shows the measurement process of part quality with a coordinate measuring machine (Zeiss Prismo Access). The Siemens controller provides the commanded position and orientation of the robot, where the end-effector refers to the tool tip. The actual pose of the tool tip is not measured directly. Instead, a target ball is mounted on the spindle housing and tracked using a laser tracker. The fixed spatial offset between the target ball and the tool tip is determined through calibration (see Figure 1B for their position), allowing computation of the actual tool tip pose from the laser tracker measurements. To quantify deviations between commanded and actual motion, the deviation is defined as the difference between the calibrated laser tracker measurements and the controller data. This calibration assumes that the offset between the target ball and tool tip remains constant, ensuring that deviation accurately reflects discrepancies between the commanded and actual end-effector positions.

The milling operation begins with the machining of a square-shaped section, progressing sequentially from the top surface at 0 mm down to -25 mm along the Z-axis. It involves a total of 25 layers, with each layer milled precisely 1

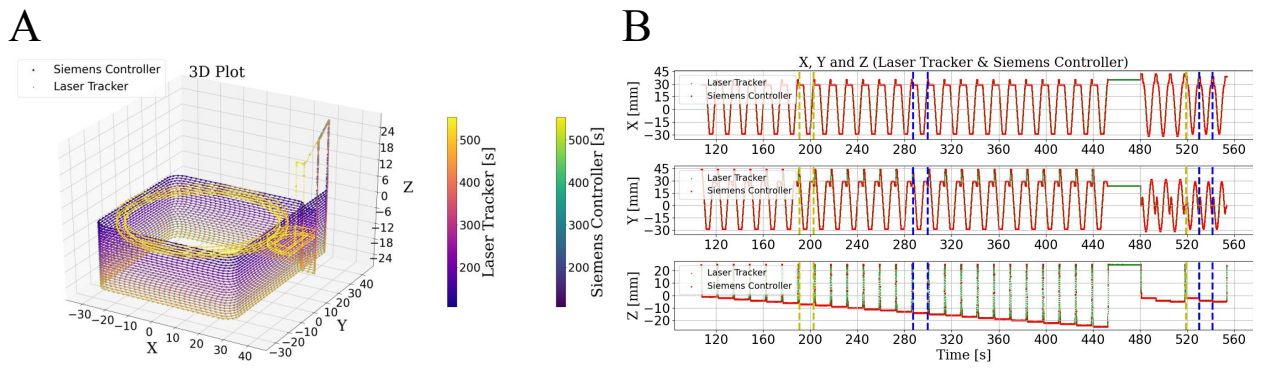

Figure 2: 2D and 3D visualizations of signals from square and circle milling operations, incorporating data from the Siemens controller and laser tracker. **A**. 3D plot showing the laser tracker and Siemens controller signals, each represented by distinct colourmaps, depicting the process from square to circle milling. **B**. Time series plots of the signals over time. The initial yellow and blue areas correspond to the square milling data at Z = -7 mm and Z = -14 mm respectively, while the subsequent yellow and blue areas indicate the circle milling data at Z = -2 mm and Z = -4 mm.

mm below the previous one. Once the square section is completed, the milling tool returns to the initial 0 mm position to commence the milling of a circular shape. This circular feature is machined in three distinct layers, with depths set at -2 mm, -4 mm and -4.8 mm respectively. After the first round of circular milling, the tool initiates a second milling sequence at the same depth increments of -2 mm, -4 mm and -4.8 mm, but this time with a reduced diameter. This repeated milling strategy with progressively smaller diameters is employed to enhance precision and minimize machining errors.

Figure 2A presents an example of a three-dimensional geometric plot illustrating the tool position during the rough milling process of a workpiece, as monitored by a laser tracker and controlled via a Siemens controller, including time information. Figure 2B complements this by providing a corresponding time series for temporal data visualization. It is organized into three subplots illustrating the variations in the X, Y and Z coordinates over time, specifically during the square and circular milling operations.

During the square milling operation, the dimensional measurements of the 7th layer (at -7 mm) and the 14th layer (at -14 mm) were precisely obtained using a coordinate measuring machine (CMM) with a volumetric accuracy of less than 3 micrometres. Similarly, the dimensional measurements for the 1st layer (at -2 mm) and the 2nd layer (at -4 mm) during the circular milling process were also acquired using the same CMM. Visual reference refers to the yellow area in Figure 2B, which indicates the dimensions corresponding to the -7 mm and -2 mm layers, and the blue area, which highlights the dimensions for the -14 mm and -4 mm layers.

A detailed visualization of the machining errors observed on the four sides of the square workpiece is presented in Figure 3A. The sides are depicted in a clockwise manner, with specific colours assigned to each: blue for the right side, orange for the front side, green for the left side, and red for the rear side. Similarly, the machining errors associated with the circular milling process, as measured by the CMM, are illustrated in Figure 3C. The zoomed-in area enhances the visualization of the geometrical discrepancies (see details in Figure 3B and 3D for error geometries in square and circle).

2.3. Methods

As outlined in the Introduction section 1, this study aims to utilize low-cost in-process laser tracker signals to predict part quality, which is normally measured using an expensive CMM. As seen in Figure 3B, the finer geometries of the four sides in square milling are different, while Figure 3D highlights the variations in the circular geometries at different locations. These inconsistencies suggest that machining errors are associated with location. Circle milling, in particular, is prone to backlash error, a phenomenon caused by the reversal motion of the robot's revolute joints. Backlash errors are observed at three distinct locations: two occurrences at $X = 0$ and one at $Y = 0, X < 0$. Since the milling process starts and ends at position ($Y = 0, X > 0$), no backlash error is present at this point. The observed backlash errors in Figure 3D are consistent with this milling pattern. This leads us to hypothesize that the angular positions of the robot joints may influence the actual machining quality. Therefore, beyond relying solely on laser

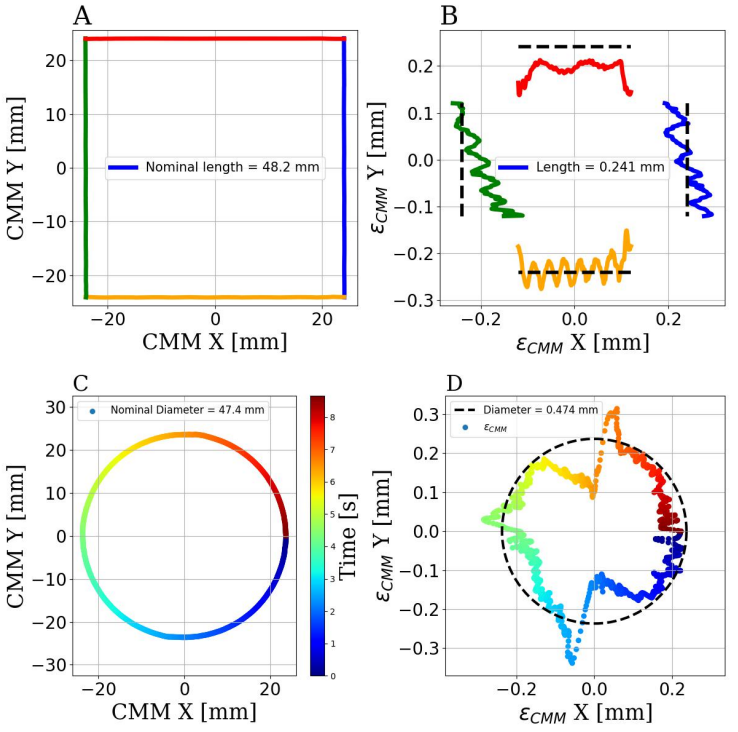

Figure 3: Geometries of part quality for square and circular features measured using CMM. **A.** Square milling geometries: the milling sequence starts at the right side (blue), moves to the front (yellow), continues to the left (green), and finishes at the rear side (red). **B.** A zoomed-in view of each side, scaled down by a factor of 200, illustrates the detailed deviation geometry. The black dashed line represents the scaled nominal size. **C.** Circular milling geometries: the milling begins at the right horizontal point and proceeds clockwise, transitioning from blue to red. **D.** ϵ_{CMM} is mapped onto a circular geometry with a scaling factor of 100 to highlight deviations. The black dashed line indicates the scaled nominal circle.

tracker signals, we incorporate additional features such as spatial coordinates and angular variations of the robot's joints during both square and circle milling to enhance the predictive model (see Figure 4A for spatial coordinates and angular changes ($\Delta\theta$) in square and circle milling.). We utilise four models to investigate which features are relevant, arising from equations 5, 6, whose functional expressions are thus represented as follows:

$$\epsilon^{(o)}_{\text{CMM}}(t) = f_o\Big[\epsilon_{\text{Laser}}(t), \dots, \epsilon_{\text{Laser}}(t-\tau)\Big] \tag{7}$$

$$\begin{aligned}\epsilon^{(a)}_{\text{CMM}}(t) = f_a\Big[&\epsilon_{\text{Laser}}(t), \dots, \epsilon_{\text{Laser}}(t-\tau),\\ &X(t), \dots, X(t-\tau),\\ &Y(t), \dots, Y(t-\tau)\Big]\end{aligned} \tag{8}$$

$$\begin{aligned}\epsilon^{(b)}_{\text{CMM}}(t) = f_b\Big[&\epsilon_{\text{Laser}}(t), \dots, \epsilon_{\text{Laser}}(t-\tau),\\ &\Delta\theta_i(t), \dots, \Delta\theta_i(t-\tau)\Big]\end{aligned} \tag{9}$$

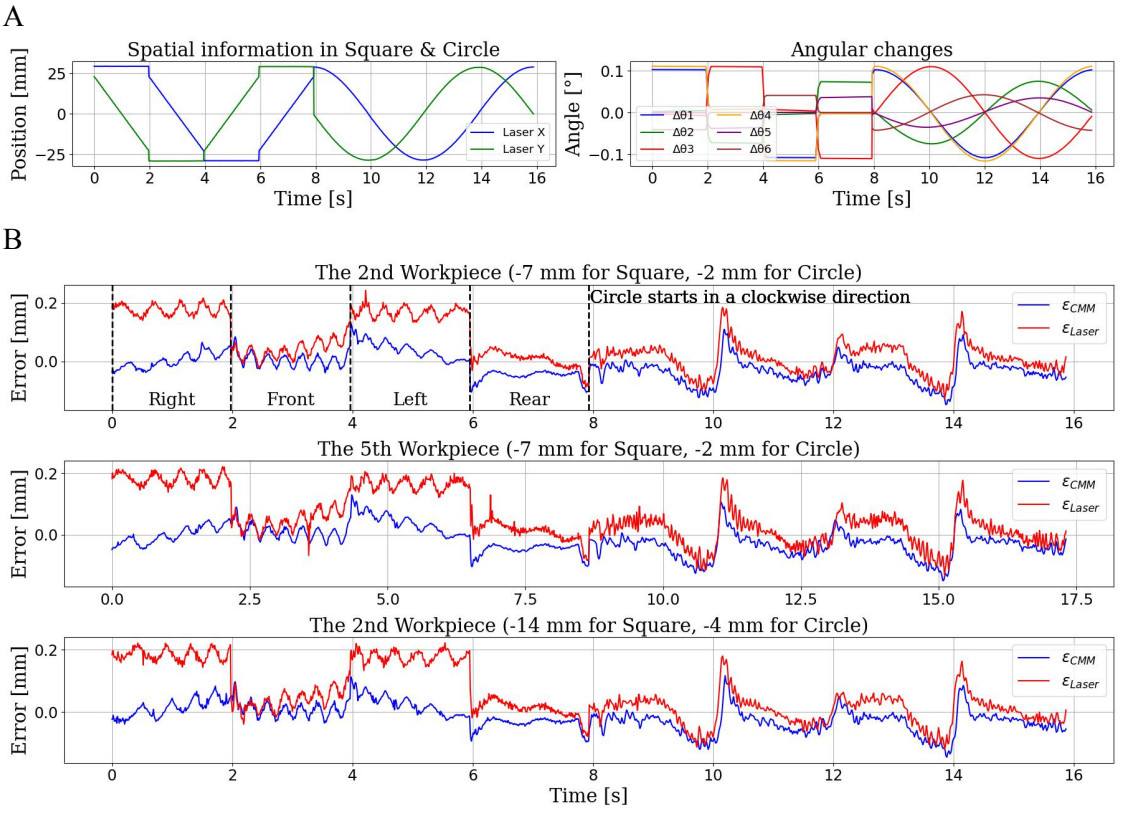

Figure 4: Input features and output targets of the data-driven model from two workpieces. Features include processed laser tracker signals (ϵ_{Laser}), spatial information (laser tracker X and Y coordinates) and angular changes of six robot joints. The target is the processed CMM data (ϵ_{CMM}). **A**. The left subplot displays the spatial trajectory of the laser tracker during the square and circle milling operations, where the X coordinates are shown in blue and the Y coordinates in green. The right subplot illustrates the angular changes in six revolute joints provided by the Siemens controller during the same milling operations. Data in **A** is derived from the 2nd workpiece, which shares a similar spatial pattern and angular changes with the 5th workpiece, differing only in milling duration. Therefore, only the 2nd workpiece data is visualized for clarifying the patterns. **B**. The top plot shows ϵ_{Laser} and ϵ_{CMM} signals for square milling followed by circle milling in the 2nd workpiece (-7 mm depth for the square and -2 mm depth for the circle). The milling sequence in the square starts from the right, followed by front, left, and rear sides, while the circle milling initiates at the horizontal right position and proceeds in a clockwise direction (refer to Figure 3 for details). The middle plot represents the same signals for the 5th workpiece (-7 mm depth in square and -2 mm depth in circle). The bottom plot displays ϵ_{Laser} and ϵ_{CMM} signals for deeper layers in the 2nd workpiece (-14 mm layer in square and -4 mm layer in circle).

$$\begin{aligned}\epsilon^{(c)}_{\text{CMM}}(t) = f_c\Big[&\epsilon_{\text{Laser}}(t), \dots, \epsilon_{\text{Laser}}(t-\tau),\\ &X(t), \dots, X(t-\tau),\\ &Y(t), \dots, Y(t-\tau),\\ &\Delta\theta_i(t), \dots, \Delta\theta_i(t-\tau)\Big]\end{aligned} \tag{10}$$

where $\epsilon^{(\cdot)}_{\text{CMM}}$ denote the model predicted machining for the errors measured by the coordinate measuring machine (CMM), relative to the nominal size, ϵ_{CMM}. The error measured by the laser tracker relative to the control command is ϵ_{Laser}. Since the control command operates at 10 Hz, which is one-tenth of the 100 Hz frequency of the laser tracker and CMM, the control command signals are upsampled to 100 Hz using linear interpolation [41] to ensure

consistency with them. The controller signals and laser tracker measurements were synchronised using a shared Unix time stamp to ensure temporal alignment. Since the controller trajectories are pre-defined and available *a priori*, linear interpolation was applied only to match the sampling rates without introducing phase shifts or timing distortions. This allows accurate computation of deviations between the commanded and measured positions while preserving the integrity of the temporal relationship between both data sources. These variables represent the primary target (ϵ_{CMM}) and feature (ϵ_{Laser}) in the model. Additionally, X and Y correspond to the spatial coordinates provided by the laser tracker, while $\Delta\theta_i$ ($i = 1, 2, ..., 6$) represents the angular changes of the robot arm's revolute joints over time (see Figure1A for six joints) that are recorded by Siemens controller. The variable t signifies the time step at which the values are taken, and τ represents the time window capturing the past time series data that influence the values at time t, a concept referred to as the causality time window. This temporal relationship accounts for the effect of prior states on the current machining error.

Following three cases in problem formulation in Section 2.1, we selected the 2nd and 5th workpieces, both of which were rough milling. In the 2nd workpiece, we extracted data at a square at -7 mm (representing the four straight sides) and a circle at -2 mm (representing the entire circle), referred to as **Data1**. Similarly, from the 5th workpiece, **Data2** was gathered from a square at -7 mm and a circle at -2 mm. Additionally, **Data3** was collected from the 2nd workpiece at a deeper square cut of -14 mm (four straight sides) and a circle at -4 mm. For model development, we trained models using **Data1** and evaluated its performance on **Data2**. Conversely, we developed further models using **Data2** and tested its performance on **Data3**. Finally, models trained on **Data2** were tested on **Data1**.

Figure 4B provides a detailed comparison of ϵ_{CMM} and ϵ_{Laser} across different workpieces, focusing on the distinct signal characteristics. Taking the top subplot in Figure 4B as an illustrative example, the signals exhibit a structured pattern when measured along the right, front, left and rear sides of the square (represented by the blue, yellow, green and red lines in Figure 3B). Subsequently, for the circular milling phase, the signals are depicted beginning from the horizontal right point, proceeding in a clockwise direction. This progression has been captured using a colour gradient (blue to red) as visualized in Figure 3D. Additionally, the middle plot in Figure 4B reveals that the 5th workpiece required a significantly longer machining duration compared to the 2nd workpiece, suggesting differences in machining dynamics or operational settings. Figure 5 uses the data from the fifth workpiece as an example to illustrate the correlation between ϵ_{CMM} and ϵ_{Laser}.

In theory, ϵ_{Laser} can be transformed through rotation and translation to match ϵ_{CMM}. However, this approach necessitates developing separate regression models for each segment, such as the right, front, left, and rear sides of the square, as well as for the four arcs of the circle (see Figure 4B for signal patterns). This is due to the varying nature of laser signal slopes—sometimes positive, sometimes negative—which may exhibit positive, negative, or no correlation with the CMM signals. The development of multiple models tailored to a particular shape is not desirable, as it cannot extend to arbitrary shape milling and thus for real-world deployment. Therefore, our objective is to develop a unified model capable of predicting the machining error across all regions.

3. Experiments and Results

3.1. Implementation

To capture complex nonlinear relationships between the input features and the target variable, we employed a diverse set of machine learning models: Decision Tree [36], Neural Network [37], Gradient Boosting [38], Random Forest [39] and K-Nearest Neighbors (KNN) [40].

This study implemented Random Forest, Decision Tree, Gradient Boosting, and KNN—using the scikit-learn library [42]. All models were trained on standardized data for consistency. The Random Forest, an ensemble method with 100 decision trees, reduces overfitting by averaging predictions. The Decision Tree constructs hierarchical decision rules to capture complex relationships. Gradient Boosting, using 100 boosting stages with a learning rate of 0.1, sequentially corrects residual errors. The KNN regressor, an instance-based approach, predicts using the average of the 5 nearest neighbours based on Euclidean distance. The neural network model used in this study was a feedforward architecture built with TensorFlow [43] and Keras [44]. It features an input layer, ten ReLU-activated hidden layers (256, 128, 128, 64, 64, 32, 32, 16, 16 and 8 neurons respectively) and a linear output layer. The model was compiled with the Adam optimizer [45] and mean squared error (MSE) as the loss function, trained 100 epochs with a batch size of 8.

We implemented four functions (see Equations 7, 8, 9 and 10 in Section 2.3) to systematically train with each of the five regression models. To rigorously examine the effects of the time window on the final model performance, we

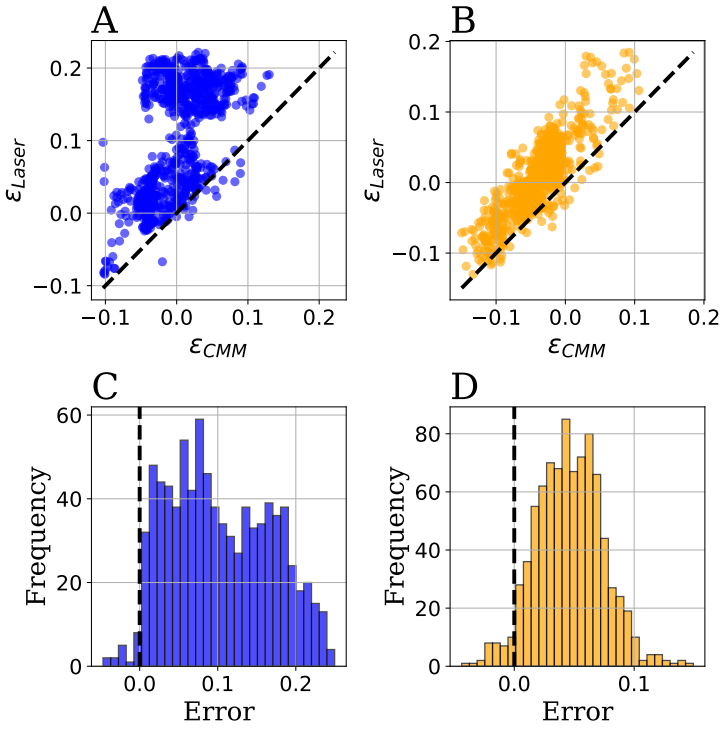

Figure 5: Data visualization and error histograms for ground truth and model input in the 5th workpiece. GT: ground truth, represented by ϵ_{CMM}; Input: main input feature represented by the laser signal, ϵ_{Laser}. Error: defined as the difference between ϵ_{Laser} and ϵ_{CMM}, i.e., Error $= \epsilon_{\text{Laser}} - \epsilon_{\text{CMM}}$. **A**. Scatter plot between GT and Input for square milling, indicating two distinct clusters and no visible correlation. **B**. Scatter plot between GT and Input for circle milling, showing a potential positive correlation. **C**. Error histogram for square milling, where the maximum error reaches 0.25 mm. **D**. Error histogram for circle milling, with a maximum error of 0.15 mm.

established a series of time windows defined as $\tau = 0, 0.01, 0.02, \ldots, 0.1$. This configuration yields a total of 11 discrete windows. Given that the processing signal operates at a frequency of 100 Hz, these time windows correspond to 0, 1, 2, ..., and 10 data points. Furthermore, recognizing the necessity for robust model validation to be consistent with the three cases in Section 2.1.1, we utilized three sets of **Training-Test** data: $\mathcal{D}_1 = \{\textbf{Data1-Data2}\}$, $\mathcal{D}_2 = \{\textbf{Data2-Data3}\}$ and $\mathcal{D}_3 = \{\textbf{Data2-Data1}\}$. This approach facilitates a more nuanced understanding of model generalizability and performance across different conditions. Consequently, this configuration resulted in the development of 440 models and 660 evaluation results, allowing for a detailed exploration of the two problems posed in Section 2.1.

3.2. Evaluation of models

Model size performance: The model will be deployed on a real robot for real-time data analysis in the future; thus, model size is a crucial factor for deployment. All models are saved as PKL files [1] for evaluation purposes.

Figure 6 presents the sizes of all 440 models. Figures 6A-E and Figures 6F-J correspond to models trained on **Data1** and **Data2** respectively. The relationship between the time window τ and model size across various models is examined. The decision tree model (Figures 6A and F) displays structural stability, although displaying a slight negative correlation, has a model size ranging from 178 kB to 179 kB for $\tau = 0$ to $\tau = 0.1$ with the minimal variation arising from the slightly higher amount of data in **Data2**. The random forest model is similarly stable, with the size variation between the maximum and minimum values being around 1%. Additionally, the model size for the random forest trained on **Data2** (Figure 6J) is slightly larger than that trained on **Data1** (Figure 6E), suggesting a dependence on training data size. In contrast, the gradient boosting model maintains a stable size regardless of the amount of training data and the length of the time window. It has the smallest size among all models, demonstrating its efficiency (see

[1] Pickle module: https://docs.python.org/3/library/pickle.html

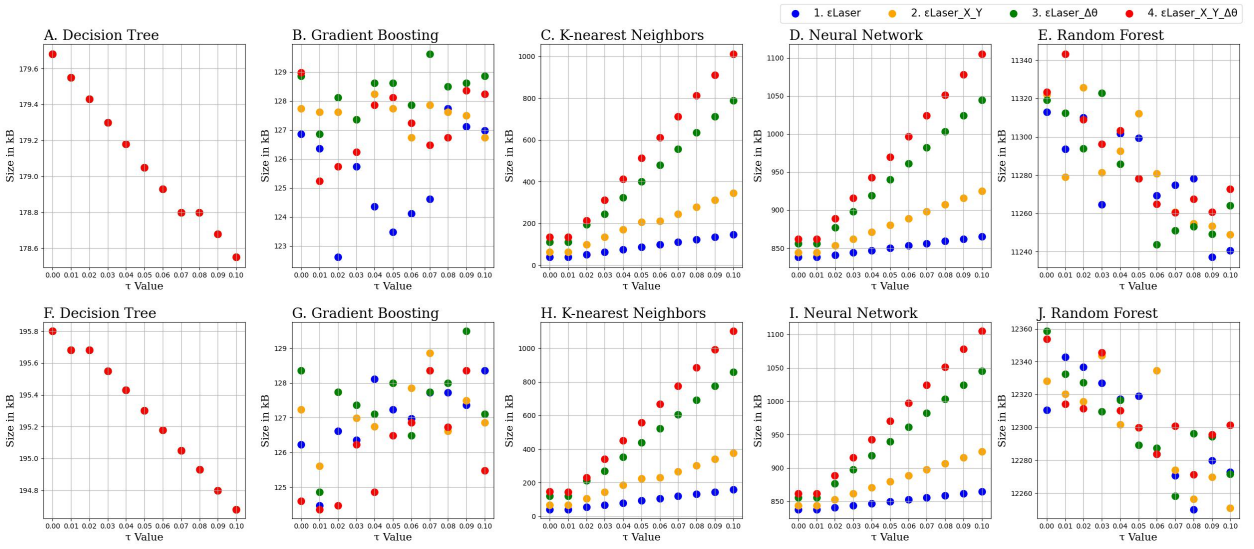

Figure 6: Model size variations in kilobytes (kB) for machine learning models across four regression functions (Equations 7, 8, 9 and 10) and eleven time window lengths (τ). **A-E** plots are for models trained on **Data1**, while **F-J** plots are for models trained on **Data2**. The X-axis is the time window length τ and the Y-axis is model size in kB. Models following Equations 7, 8, 9 and 10 are represented using blue, yellow, green, and red scatter plots, respectively. In **A** and **F**, only red scatter points are visible due to the overlap of all colours, as the Decision Tree models gives nearly identical sizes across all feature combinations.

Figures 6B and G). The KNN and neural network models exhibit a clear positive correlation between model size and the time window length τ. Particularly for the KNN model, the size at $\tau = 0.1$ is five times larger than at $\tau = 0$ (1000 kB vs. 200 kB, shown in red markers). The neural network also shows an increasing trend, although not as pronounced as that in the KNN (see Figures 6C, D, H and I).

In Figure 6, the blue scatter corresponds to models utilizing a single feature (ϵ_{Laser}), the yellow scatter represents models with three features (ϵ_{Laser}, X, and Y), the green scatter indicates models using seven features (ϵ_{Laser}, $\Delta\theta_1$, $\Delta\theta_2$, $\Delta\theta_3$, $\Delta\theta_4$, $\Delta\theta_5$, $\Delta\theta_6$), while the red scatter incorporates all nine features (ϵ_{Laser}, X, Y, $\Delta\theta_1$, $\Delta\theta_2$, $\Delta\theta_3$, $\Delta\theta_4$, $\Delta\theta_5$, $\Delta\theta_6$). This increase in the number of features contributes to the observed increase in model size from blue, to yellow, to green and finally to red in the KNN and neural network models as would be expected. Overall, considering the impact of time window length, model size scale, and stability relative to the training data volume, the gradient boosting model is recommended as the optimal candidate in terms of model size, outperforming the others in this investigation.

Model accuracy metrics: The mean absolute error (MAE $= \frac{1}{N}\sum_{i=1}^{N}|y_i - \hat{y}_i|$) and the root mean squared error (RMSE $= \sqrt{\frac{1}{N}\sum_{i=1}^{N}(y_i - \hat{y}_i)^2}$) are utilized as prediction performance measures with units in mm. Figure 7 illustrates the performance of the models across 11 time windows using 4 distinct regression functions (see Equations 7, 8, 9 and 10 in Section 2.3) for the 5 machine learning models using three sets of training-test data pairs, i.e., $\mathcal{D}_1$ (Figures 7A - E), $\mathcal{D}_2$ (Figures 7F - J) and $\mathcal{D}_3$ (Figures 7K - O).

Figure 7C shows successful demonstration of the first scenario of the first research problem, in which the KNN model trained on data from one work piece accurately predicts values when applied to a different workpiece achieving an MAE of 0.0095 and an RMSE of 0.0146. Figures 7C and 7H illustrate the second scenario of the first research problem, where the KNN model maintains prediction accuracy across different layers, achieving an MAE of 0.0095 and RMSE of 0.0146 in Figure 7C, and an MAE of 0.0146 and RMSE of 0.0202 in Figure 7H. Finally, Figures 7C and 7M present the third scenario, indicating that the KNN model, recognized as the best performer, exhibits prediction accuracy independent of which dataset was used for training, with an MAE of 0.0095 and RMSE of 0.0146 for Figure 7C and an MAE of 0.0088 and RMSE of 0.0138 for Figure 7M.

Analysis of the second research problem showed that the inclusion of spatial information and angular positions generally enhances model performance compared to using only ϵ_{Laser} (see blue lines in all subfigures in Figure 7). Furthermore, among the four regression functions, the addition of spatial information (X and Y coordinates) yields the

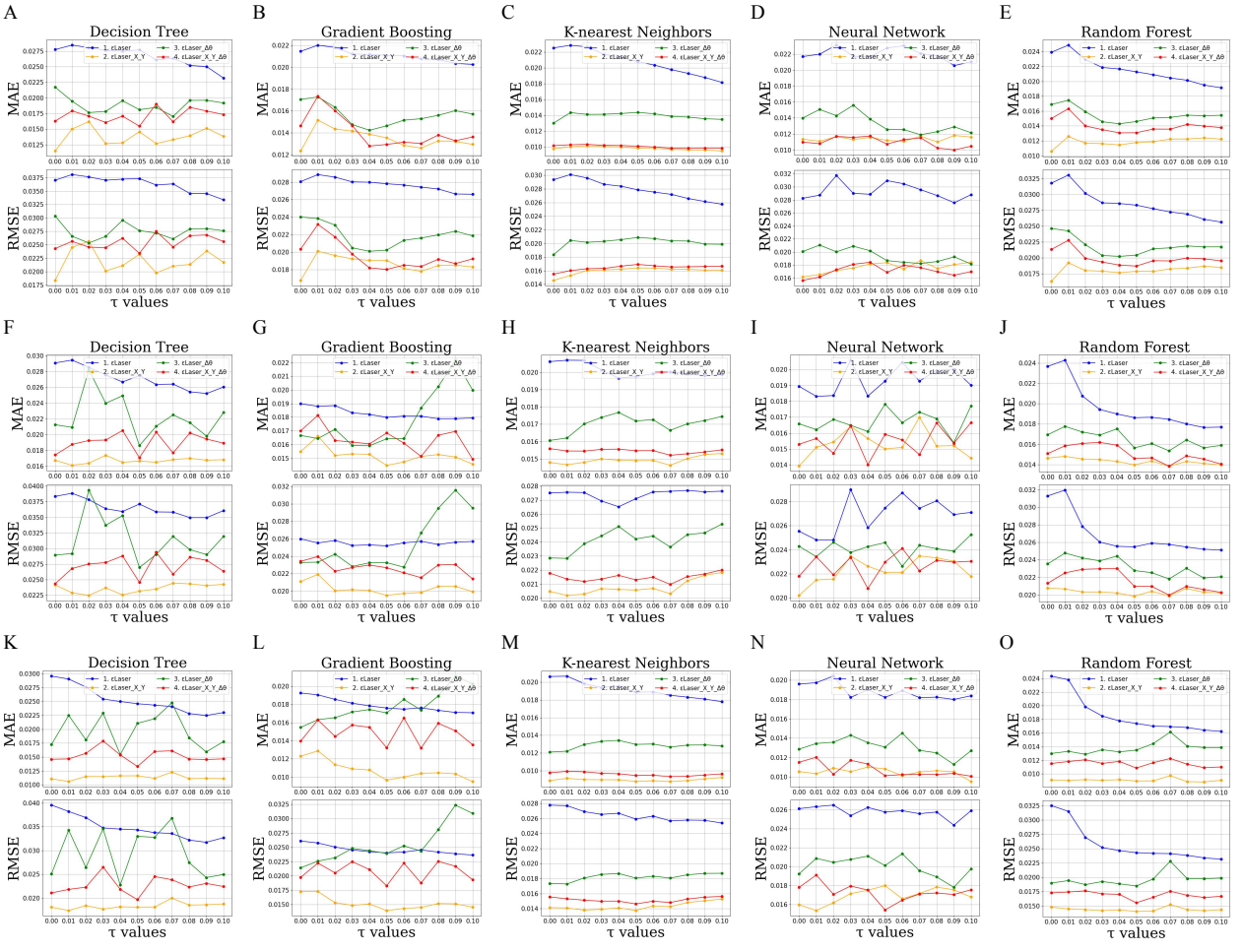

Figure 7: Regression metrics for machine learning models across four regression functions (Equations 7, 8, 9, and 10) and eleven time window lengths (τ). **A-E** display results for Decision Tree, Gradient Boosting, K-Nearest Neighbors, Neural Network, and Random Forest models developed on $\mathcal{D}_1$, **F-J** show results for $\mathcal{D}_2$, while **K-O** show results for $\mathcal{D}_3$. Blue, yellow, green, and red line charts indicate models based on Equations 7, 8, 9, and 10, respectively. Each subfigure includes two plots representing MAE and RMSE. Lower values are preferable for MAE and RMSE.

best performance. This is evidenced by the yellow lines in subplots, which almost always has lower values compared to the other three. Lastly, the overall performance of the regression functions, ranked from highest to lowest, is as follows: (1) ϵ_{Laser} combined with the spatial information of X and Y coordinates, (2) ϵ_{Laser} with the spatial information of X and Y coordinates along with the angular changes of six revolute joints, (3) ϵ_{Laser} combined with the angular changes of six revolute joints, and (4) ϵ_{Laser} alone, as observed in Figures 7A-O.

In the next section, the trained machine learning models will be evaluated based on their performance in predicting dimensions for milling of square and circular shapes.

3.3. Dimensional error prediction

All machine learning models developed using $\mathcal{D}_1$ at $\tau = 0$ were evaluated, as this produced optimal results for most regression functions. ML predictions overlaid on the ground truth are shown in Figure 8 for square shape (ϵ_{CMM}) prediction and Figure 9 for circle shape (ϵ_{CMM}) prediction. The configuration of these figures aligns with Figure 3B and Figure 3D. Among all machine learning models, KNN demonstrates a with $\tau = 0$ gives the best performance in terms of both MAE and RMSE (see Table 1) and also seen in the second row of Figures 8, 9, associated with Equation 8 which uses ϵ_{Laser} data combined with the spatial information of X and Y coordinates. Figure 10 illustrates the time-series performance of the best performing K-Nearest Neighbors model utilizing $\mathcal{D}_1$ at $\tau = 0$ for the four

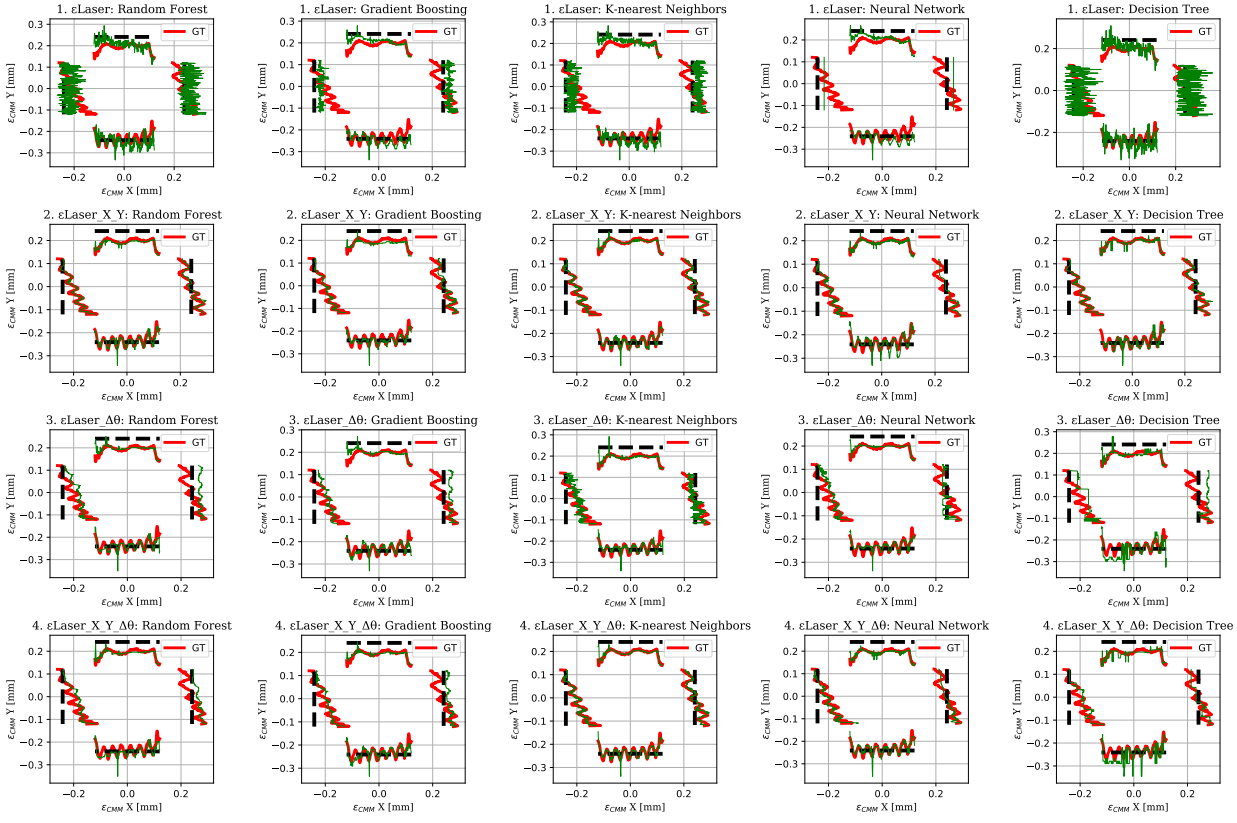

Figure 8: Machine learning predictions (at $\tau = 0$) vs. ground truth in square geometries. The ground truth is represented by wide red lines, while ML predictions as green lines. Models are based on Equations 7, 8, 9 and 10 in subfigures entitled with 1. ϵ_{Laser}, 2. ϵ_{Laser} X Y, 3. ϵ_{Laser} $\Delta\theta$ and 4. ϵ_{Laser} X Y $\Delta\theta$ respectively.

regression functions represented by Equations 7, 8, 9, and 10. Among these, models based on Equation 8 achieved the best performance, and therefore, Equation 8 is selected for further analysis of dimensional error prediction.

Figure 11 presents a detailed comparison between the ground truth, denoted as ϵ_{CMM}, and the corresponding values from either the machine learning (ML) models or the raw sensor measurement ϵ_{Laser}. In particular, Figure 11A reveals a multimodal data distribution, where the data are segregated into two distinct groups divided by a threshold value of 0.1 in ϵ_{Laser}. For values below this threshold, an increase in ϵ_{CMM} is accompanied by an increase in ϵ_{Laser}; however, the relationship exhibits a shift and does not lie along the diagonal line. In contrast, for ϵ_{Laser} values above 0.1, the sensor measurement remains approximately constant irrespective of increases in ϵ_{CMM} suggestive of no correlation between the data. Hence, the laser sensor cannot be used directly as a measure of the part dimensional error. The implementation of machine learning techniques (Figures 11B-E) mitigates this discrepancy where it can be seen that the error scatter is clustered along the diagonal line. This improvement is further substantiated by Figure 12, which depicts the error histogram. Here, the error is defined as the difference between either the sensor measurement or the ML prediction and the ground truth (ϵ_{Laser}/ML prediction $- \epsilon_{\text{CMM}}$). Notably, the introduction of the ML models reduces the maximum error from approximately 0.25 mm, as observed with ϵ_{Laser}, to about 0.05 mm. This fivefold improvement in error reduction illustrates the enhanced accuracy and reliability provided by the ML approach.

Using the machine learning models and ϵ_{Laser}, dimensional metrics were computed for both square and circular features. For the square (in the coordinate scale $[-23, 23]$ mm), the X and Y dimensions were defined as $X = x_{\text{right}} - x_{\text{left}}$ and $Y = y_{\text{front}} - y_{\text{rear}}$, respectively. Deviations from the nominal size were computed as $X_{\text{dev}} = X - X_{\text{nom}}$ and $Y_{\text{dev}} = Y - Y_{\text{nom}}$, while prediction errors relative to ground truth (GT) were $X_{\text{err}} = X_{\text{pred}} - X_{\text{GT}}$ and $Y_{\text{err}} = Y_{\text{pred}} - Y_{\text{GT}}$. For the circle, the predicted diameter D was evaluated, with deviation $D_{\text{dev}} = D - D_{\text{nom}}$ and error to ground truth $D_{\text{err}} = D_{\text{pred}} - D_{\text{GT}}$. In predicting the X direction dimension size, the decision tree emerges as the most effective model,

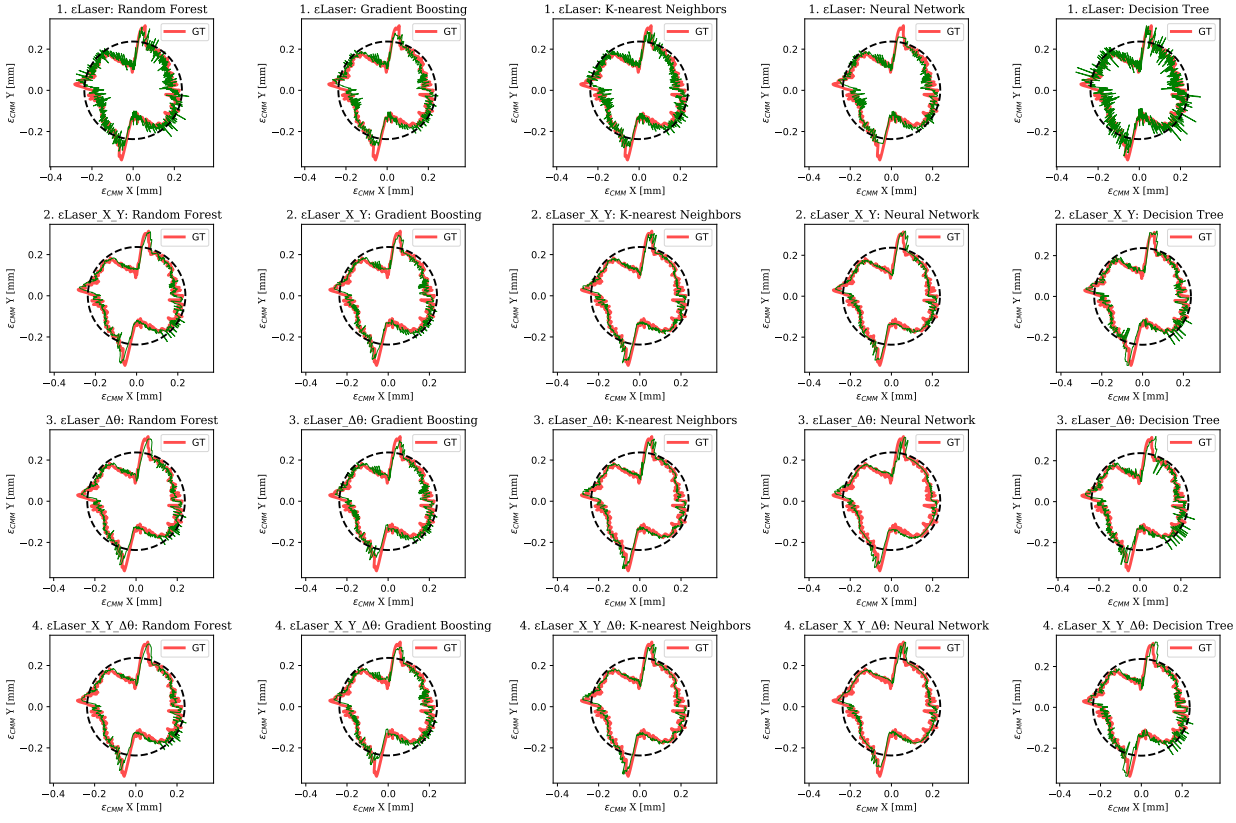

Figure 9: Machine learning predictions vs. ground truth in circle geometries prediction at $\tau = 0$. The ground truth is represented by wide red lines with partial transparency, while ML predictions are shown as thin lines in green. Models are based on Equations 7, 8, 9 and 10 in subfigures entitled with 1. ϵ_{Laser}, 2. ϵ_{Laser} X Y, 3. ϵ_{Laser} $\Delta\theta$ and 4. ϵ_{Laser} X Y $\Delta\theta$ respectively.

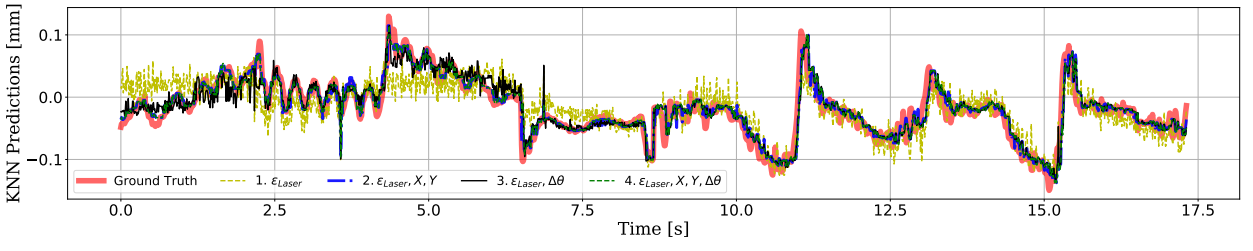

Figure 10: K-Nearest Neighbors predictions compared to ground truth over milling time with $\tau = 0$. The ground truth is in red solid lines, while the predictions are in distinct colours: Equation 7 (yellow dashed line), Equation 8 (blue dash-dot line), Equation 9 (black solid line) and Equation 10 (green dashed line).

while the random forest leads to accuracy for predicting the Y direction dimension size. Additionally, gradient boosting surpasses the other models in predicting circle diameter (for further details, refer to Table 2). The X (Right-Left), Y (Front-Rear), and Diameter values represent the mean predictions aggregated across the entire dataset. Other metrics presented in Table 2 are calculated based on these mean values. A comprehensive view of the data distribution refers to the violin plots in Figure 13 and Figure 14. Based on visual assessment, the patterns of the violin plots for KNN and gradient boosting closely resemble the ground truth as measured from the CMM in the distribution of circle diameter data (see Figure 14). For square dimension prediction, the decision tree exhibits strong similarity to the ground truth in

Table 1
The table gives performance metrics (MAE and RMSE in mm) for machine learning models, computed from the ground truth ϵ_{CMM} and model predictions. Models were developed with data $\mathcal{D}_1$ and Equation 8 associated with optimal feature combination for $\tau = 0, 0.01, 0.04, 0.07, 0.10$. The machine learning models are: Decision Tree (DT), Neural Network (NN), Gradient Boosting (GB), Random Forest (RF), and K-Nearest Neighbors (KNN). The MAE and RMSE between ϵ_{Laser} and ϵ_{CMM} are 0.0756 and 0.0943 respectively, serving as a baseline for comparison.

τ	Metrics	RF	GB	KNN	NN	DT
0	MAE	0.0106	0.0123	**0.0097**	0.0114	0.0115
	RMSE	0.0163	0.0168	**0.0146**	0.0162	0.0184
0.01	MAE	0.0111	0.0126	0.0152	0.0100	0.0150
	RMSE	0.0165	0.0192	0.0201	0.0153	0.0245
0.04	MAE	0.0116	0.0114	0.0139	0.0100	0.0128
	RMSE	0.0182	0.0176	0.0190	0.0162	0.0211
0.07	MAE	0.0117	0.0122	0.0126	0.0097	0.0133
	RMSE	0.0187	0.0182	0.0178	0.0162	0.0210
0.10	MAE	0.0116	0.0122	0.0129	0.0095	0.0138
	RMSE	0.0184	0.0185	0.0183	0.0161	0.0217

Table 2
Metrics for dimensional error prediction using machine learning models are shown. Square nominal size is 48.2 mm, and the nominal diameter for circles is 47.4 mm, with upper and lower tolerances of $\pm$ 0.15 mm. Ground Truth is denoted as GT, Random Forest as RF, Decision Tree as DT, Gradient Boosting as GB, K-nearest Neighbors as KNN, and Neural Network as NN. All measurements are in millimeters (mm), and results are rounded to four decimal places, with the best performance metrics highlighted in bold. The machine learning models were developed using $\mathcal{D}_1$ based on Equation 8 at $\tau = 0$.

	Square						Circle		
	X (Right-Left)	Y (Front-Rear)	X Deviation	Y Deviation	X Error to GT	Y Error to GT	Diameter	Diameter Deviation	Error to GT
GT	48.1617	48.1426	-0.0383	-0.0574	0	0	47.3266	-0.0734	0
ϵ_{Laser}	48.2178	48.1608	0.0178	-0.0392	0.0561	0.0182	47.4188	0.0188	0.0922
RF	48.1628	48.1427	-0.0372	-0.0573	0.0011	**0.0001**	47.3297	-0.0703	0.0031
GB	48.1662	48.1422	-0.0338	-0.0578	0.0045	-0.0004	47.3288	-0.0712	**0.0022**
KNN	48.1644	48.1443	-0.0356	-0.0557	0.0027	0.0017	47.3305	-0.0695	0.0039
NN	48.1643	48.1407	-0.0357	-0.0593	0.0026	-0.0019	47.3293	-0.0707	0.0027
DT	48.1619	48.1447	-0.0381	-0.0553	**0.0002**	0.0021	47.3298	-0.0702	0.0032

the X direction, while the random forest aligns closely with the ground truth in the Y direction (see Figure 13). These observations are consistent with the metrics presented in Table 2.

3.4. Computational efficiency analysis

An offline latency and energy analysis was conducted to evaluate the real-time feasibility of the proposed models. The best-performing configuration, using the K-nearest Neighbours model with ϵ_{laser} and X/Y position inputs at $\tau = 0$ (MAE = 0.0097 mm and RMSE = 0.0146 mm), achieved an inference latency of 1.37 ± 0.13 ms (Median $\pm$ SD) across 100 inferences and an energy consumption of 53 mJ per inference on an AMD Ryzen 7 7700X CPU. These results confirm that the inference time is well within the 10 ms sampling interval of the 100 Hz laser tracker and the 100 ms cycle of the 10 Hz controller, indicating that the proposed approach satisfies real-time operational requirements.

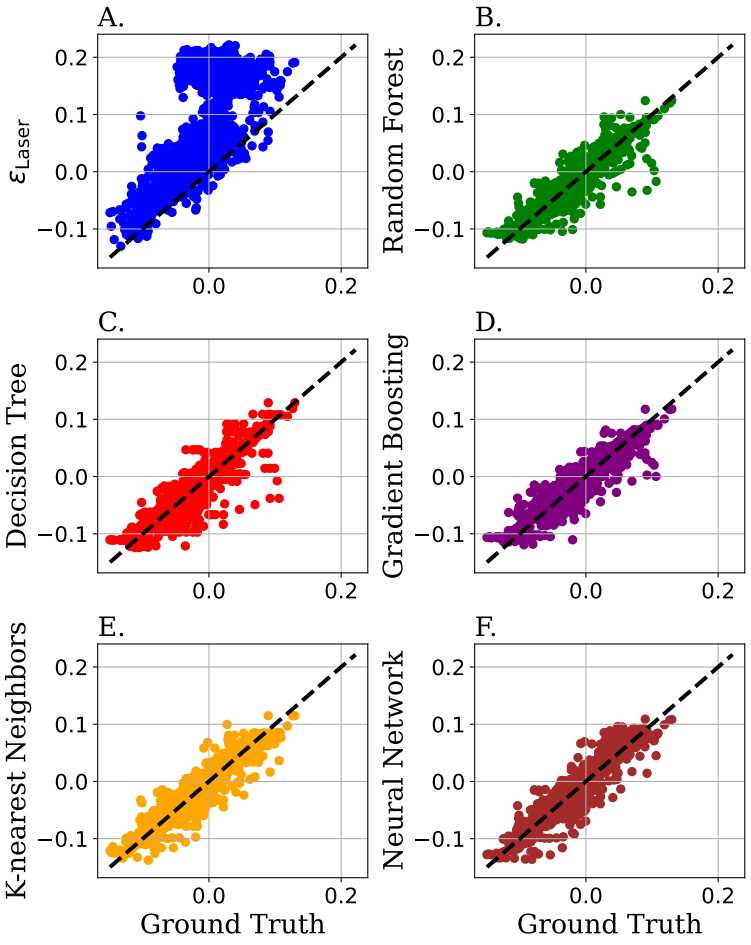

Figure 11: Scatter plots depicting the relationship between ground truth and machine learning predictions/model inputs. The data is aggregated from both square and circle milling signals. The difference between the ground truth and model input is illustrated in blue, while predictions from the random forest, decision tree, gradient boosting, K-nearest neighbors, and neural network are represented in green, red, purple, orange, and brown, respectively. All models were developed on $\mathcal{D}_1$ using Equation 8 at $\tau = 0$.

4. Discussion

The study involved consideration of multiple scenarios. The first research question of predicting the CMM measurements of part quality using laser tracker data were examined. These validated that the model trained on one work piece from one layer of machining could predict successfully on another work piece and for different layers, nor is it sensitive to which work piece data is used to build models. For the second question, we confirmed that incorporating spatial information and the angular changes of robot joints improves prediction performance. The performance hierarchy is as follows:

$\mathbb{E}\left[\|\hat{\epsilon}_{CMM}\| \mid \epsilon_{\text{Laser}}, \mathbf{X}, \mathbf{Y}\right] > \mathbb{E}\left[\|\hat{\epsilon}_{CMM}\| \mid \epsilon_{\text{Laser}}, \mathbf{X}, \mathbf{Y}, \Delta\theta_{1:6}\right] > \mathbb{E}\left[\|\hat{\epsilon}_{CMM}\| \mid \epsilon_{\text{Laser}}, \Delta\theta_{1:6}\right] > \mathbb{E}\left[\|\hat{\epsilon}_{CMM}\| \mid \epsilon_{\text{Laser}}\right]$

indicating that the inclusion of spatial information alongside ϵ_{Laser} yields the best performance. This study demonstrated that the proposed machine learning methods significantly enhanced error prediction accuracy as measured by the mean absolute error (MAE) compared to using only laser tracker data, achieving a seven-fold improvement from 0.0756 mm to 0.0097 mm, particularly for square and circular geometrical shapes, with a precision of less than 100 micrometres.

The results indicate that the best prediction performance is achieved by using the laser-measured deviations (ϵ_{laser}) together with the X and Y coordinates of the tool, without including joint angular variations. This can be attributed

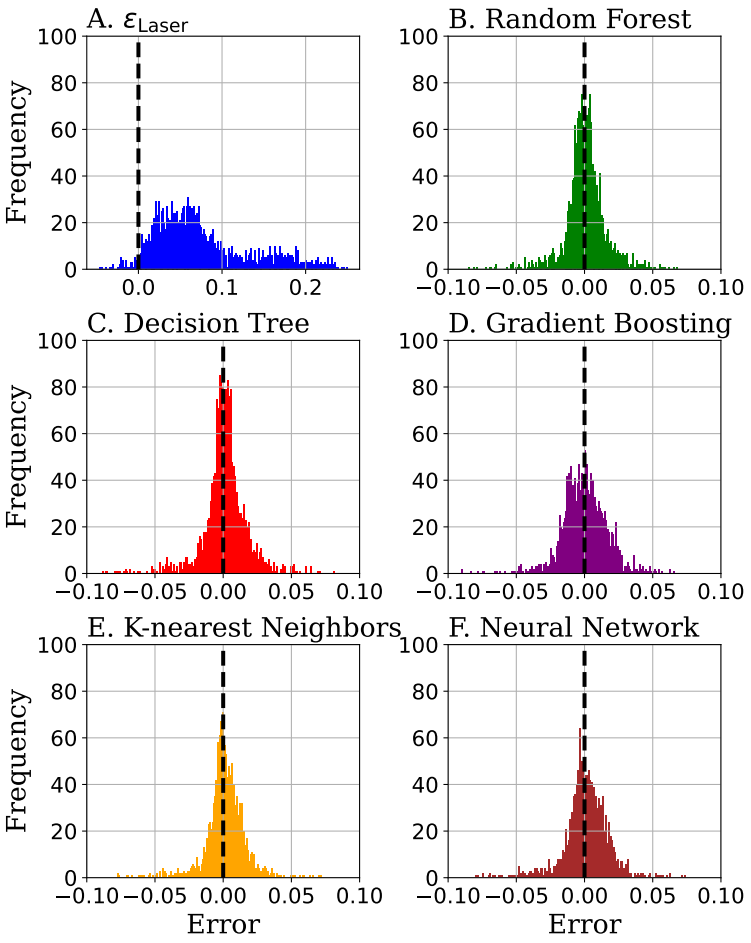

Figure 12: Error histograms illustrating the discrepancies between ground truth and machine learning predictions/model inputs. The data is aggregated from both square and circle milling signals. The difference between the ground truth and model input is depicted in blue, while the differences for predictions from the Random Forest, Decision Tree, Gradient Boosting, K-nearest Neighbors, and Neural Network models are represented in green, red, purple, orange, and brown, respectively. All models were developed using $\mathcal{D}_1$ based on Equation 8 at $\tau = 0$.

to the spatial dependence of machining errors. Systematic deviations such as gravitational sag, structural compliance, and fixture deformation primarily vary with the tool's position in the workspace. Joint angles, which describe the robot configuration in joint space, relate to tool-tip deviations only indirectly and nonlinearly. Including joint angles therefore provides limited additional information and may introduce redundancy or noise. As a result, the combination of ϵ_{laser} with X–Y positions captures the most relevant information for accurate machining error prediction.

An additional noteworthy observation is that the model performance may be affected by the phase shift between the training and test signal data; however, configuring an appropriate time window may help mitigate this effect and enhance performance. As illustrated in Figure 4B, **Data1** (top plot) and **Data2** (middle plot) show no lag (phase shift) after applying cross-correlation [46], whereas a phase shift is present between **Data2** (middle plot) and **Data3** (bottom plot) on the left and right sides during square milling. This is attributed to the fact that **Data1** and **Data2** are derived from the same layer (-7 mm), while **Data3** is obtained from a different layer (-14 mm). Figures 7A-E, which present the models trained on **Data1** and tested on **Data2**, indicate no phase shift; thus, the optimal performance for all machine learning models, developed using the best regression function (Equation 8), occurs at $\tau = 0$. Among these models, the KNN algorithm exhibits the best performance. In contrast, Figures 7F-J depict models trained on **Data2** and tested on **Data3**, where a phase shift is evident on the left and right sides during square milling. Consequently, the optimal performance of all machine learning models, developed using the same regression function (Equation 8),

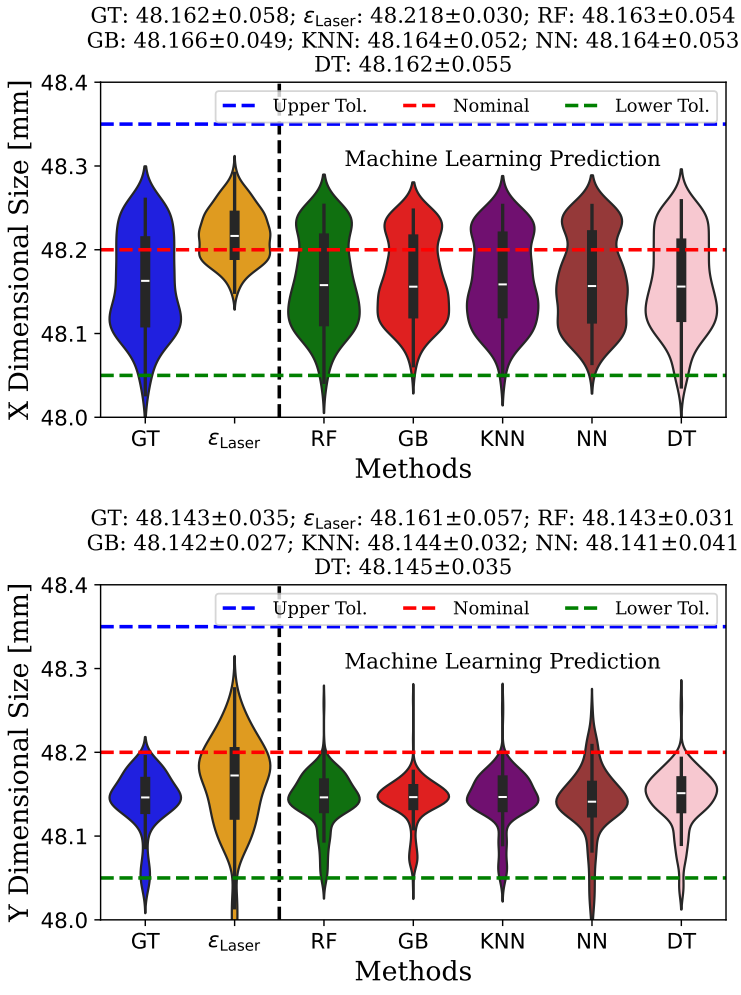

Figure 13: The data distribution for the X and Y direction dimensions in square milling, derived from model inputs (processed laser tracker signals) and machine learning predictions, is presented alongside the real dimensions of the milled part depicted in the ground truth subplot. The machine learning models were developed using $\mathcal{D}_1$ based on Equation 8 at $\tau = 0$. Additionally, the mean and standard deviation of the dimensions are provided in the subfigure captions. The upper tolerance, nominal size and lower tolerance are represented by blue, red and green dashed lines.

does not occur at $\tau = 0$. This may be due to nonlinear effects such as backlash that has dependency on the system memory or equivalently past position data. The relationship between the time window and phase shift requires further investigation in future studies, this is beyond the current study's scope and will be addressed in future work with a more comprehensive experimental setup and data.

While the model performed well, the limited data for irregular geometries may constrain its applicability to more complex shapes. In future work, we aim to establish uniform rules that can be generalized to any random geometries, extending beyond just milling circles and squares. This will involve examining a variety of regular and irregular shapes and configurations to gain insights into the principles governing dimensional error prediction across diverse scenarios. By incorporating a broader spectrum of geometric forms—including the X and Y directions of ϵ_{Laser} for both regular and irregular shapes—into the dataset and correlating them with the X and Y directions of ϵ_{CMM}, we aim to identify and create generalised feature sets. This approach is intended to establish a consistent approach that enhances the model's robustness and accuracy to any shape being manufactured.

The study is also limited to experiments conducted on a single robot (KUKA KR210), under a specific working condition, and with simple square and circular workpieces, using a relatively small number of training data sets. Despite

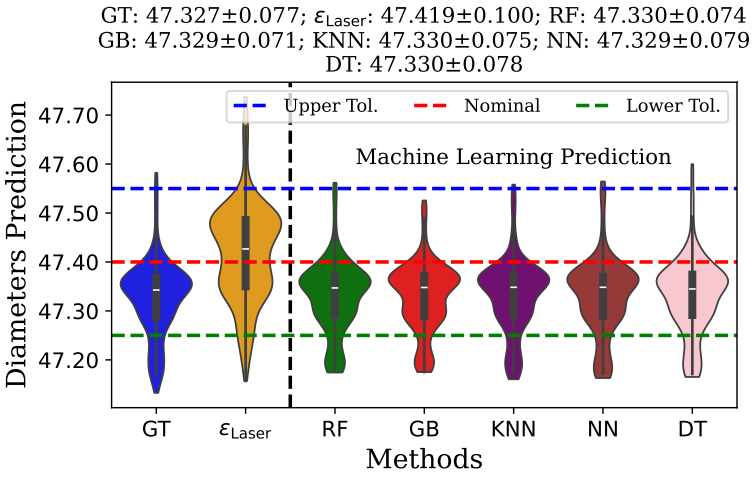

Figure 14: The figure illustrates the data distribution of diameter dimensions in circle milling, which is based on model inputs (processed laser tracker signals) and machine learning predictions, alongside the actual dimensions of the milled part shown in the ground truth subplot. The machine learning models were developed using $\mathcal{D}_1$ following Equation 8 at $\tau = 0$. The mean and standard deviation of the dimensions are also included in the figure captions. The upper tolerance, nominal size and lower tolerance are represented by blue, red and green dashed lines.

these constraints, the results demonstrate that in-process fusion of laser tracker and controller signals can accurately predict machining errors and provide practical insights when multiple parts of the same geometry are manufactured, having learned from a single part process. Cross-workpiece and cross-layer evaluations indicate that models trained on the same machining layers generalise well across different workpieces (MAE $\approx$ 0.01 mm), while performance across different layers shows a modest degradation (MAE $\approx$ 0.015 mm) yet remains within practically useful limits. Extending this approach to a broader range of robots, toolpaths, and free-form surfaces will require additional training data and could benefit from incorporating physics-informed model structures that reflect kinematic and compliance relationships. In an industrial setting, the predictive model can be integrated with offline measurements, focusing detailed inspection on regions with high predictive uncertainty, and using the resulting data to iteratively update the model. These considerations provide a realistic pathway for translating the current proof-of-concept into broader industrial applications.

Coordinate Measuring Machines (CMMs) serve not only for quality inspection but also for product authentication, and thus cannot be entirely replaced by predictive models. The proposed approach is intended to complement, rather than substitute, traditional CMM-based verification by providing accurate in-process error prediction that can reduce the frequency of offline inspections and associated non-value-added time. While laser trackers are not necessarily lower in cost than CMMs, their strength lies in flexibility and the ability to capture dynamic tool and workpiece behaviour during machining, capabilities beyond those of conventional inspection systems. Therefore, this study is to demonstrate a practical and effective pathway toward integrating predictive, metrology-driven monitoring into robotic manufacturing, thereby enhancing process efficiency and reducing the verification cost of manufacturing without claiming full replacement of existing inspection technologies.

While the current study focuses on predictive modelling and does not yet implement closed-loop error compensation, it provides a solid foundation for achieving such capability in future research. Real-time compensation requires additional developments, including seamless integration of the predictive model into the robot controller, ensuring low-latency data processing, and evaluating whether the robot's control frequency (10 Hz) is sufficient to apply timely corrections. Addressing these challenges will enable the extension of the proposed framework from real-time error prediction to active error compensation, ultimately supporting autonomous, metrology-driven robotic machining.

5. Conclusion

In this study, machine learning-based quality prediction methods for milling processes were developed and evaluated. The real quality of milled parts was assessed using a coordinate measuring machine and then linked with low-cost, in-process sensing signals collected from a laser tracker to build a data-driven model. While the laser tracker signals are theoretically expected to be identical to part quality, in practice, they only demonstrate a partial correlation. The developed algorithm leveraged these predicted machining errors to estimate the dimensional properties of square and circular features and compared them to actual measurements. To capture the effect of past machining actions on current results, a time window approach was implemented to aggregate historical machining errors and corresponding sensing signals. Furthermore, four groups of features were designed, incorporating spatial tool positions and angular variations of robot joints, to enhance the prediction accuracy.

Machine learning algorithms— Decision Tree, Gradient Boosting, K-nearest Neighbors (KNN), Neural Network, and Random Forest—were compared based on model size, performance metrics, and machining error prediction. Although KNN showed the highest accuracy in regression, its model size varied significantly with increased features and training data volume, thus potentially impacting its deployment in real-world scenarios. Gradient Boosting, in contrast, achieved comparable accuracy and dimensional prediction while maintaining a stable model size regardless of time windows or data volume, making it the preferred choice. Finally, the data-driven algorithm was evaluated across different workpieces and spatial locations, demonstrating a sevenfold error reduction, from 0.0756 mm using laser data to 0.0097 mm in mean absolute error using the proposed data-driven models. This study has demonstrated and validated the feasibility of using low-cost in-process sensing signals to predict costly CMM data, enabling fast inspection of part quality and significantly reducing costs.

Building upon the findings of this study, future research will investigate the application of advanced deep learning architectures, such as CNN-LSTM [47] and Transformer [48] models, which have demonstrated strong capabilities in modeling temporal dependencies and complex feature interactions. While the present work focused on establishing the feasibility of predicting CMM measurement data from in-process signals using conventional machine learning models and feedforward neural networks, the results confirm the existence of strong nonlinear correlations between these data sources. Incorporating architectures with enhanced time-series modeling capabilities may further improve prediction accuracy and robustness, offering potential for more effective reduction of CMM inspection in precision manufacturing.

Acknowledgement

This work was supported by UK Engineering and Physical Sciences Research Council EP/P006930/1.

Declaration of competing interest

The authors declare that they have no known competing financial interests or personal relationships that could have appeared to influence the work reported in this paper.

CRediT authorship contribution statement

Chaoyue Niu: Conceptualization, Methodology, Software, Validation, Formal analysis, Writing - Original draft preparation. **Bin Chen:** Formal analysis, Software, Validation, Writing - review and editing. **Simon Fletcher:** Investigation (machining trials), Data Curation, Writing - review and editing. **Peace Onawumi:** Investigation (machining trials), Data Curation, Writing - review and editing. **Erdem Ozturk:** Investigation, Writing - review and editing. **Mahdi Mahfouf:** Supervision, Funding acquisition, Writing - review and editing. **Visakan Kadirkamanathan:** Conceptualization, Supervision, Project administration, Funding acquisition, Visualization, Writing - review and editing.

References

[1] M. Eberhardt, F. Teal, Productivity analysis in global manufacturing production. (2010).
[2] N. Anumbe, C. Saidy, R. Harik, A primer on the factories of the future, Sensors 22 (15) (2022) 5834.

[3] V. D. Majstorovic, N. Durakbasa, Y. Takaya, S. Stojadinovic, Advanced manufacturing metrology in context of industry 4.0 model, in: Proceedings of the 12th International Conference on Measurement and Quality Control-Cyber Physical Issue: IMEKO TC 14 2019 12, Springer, 2019, pp. 1–11.
[4] Z. Zerun, T. Xiaowei, C. Chen, P. Fangyu, Y. Rong, Z. Lin, L. Zepeng, W. Jiawei, High precision and efficiency robotic milling of complex parts: Challenges, approaches and trends, Chinese Journal of Aeronautics 35 (2) (2022) 22–46.
[5] Z. Wang, R. Zhang, P. Keogh, Real-time laser tracker compensation of robotic drilling and machining, Journal of Manufacturing and Materials Processing 4 (3) (2020) 79.
[6] R. J. Hocken, P. H. Pereira, et al., Coordinate measuring machines and systems, Vol. 6, CRC press Boca Raton, FL, USA:, 2012.
[7] D. Bernd, M. Henriette, H. Gross, et al., Handbook of optical systems, volume 5: Metrology of optical components and systems, John Wiley & Sons, 2012.
[8] P. Blecha, M. Holub, T. Marek, R. Jankovych, F. Misun, J. Smolik, M. Machalka, Capability of measurement with a touch probe on cnc machine tools, Measurement 195 (2022) 111153.
[9] S. Ibaraki, Y. Kimura, Y. Nagai, S. Nishikawa, Formulation of influence of machine geometric errors on five-axis on-machine scanning measurement by using a laser displacement sensor, Journal of Manufacturing Science and Engineering 137 (2) (2015) 021013.
[10] B. Li, F. Li, H. Liu, H. Cai, X. Mao, F. Peng, A measurement strategy and an error-compensation model for the on-machine laser measurement of large-scale free-form surfaces, Measurement Science and Technology 25 (1) (2013) 015204.
[11] D. Ding, Z. Zhao, R. Huang, C. Dai, X. Zhang, T. Xu, Y. Fu, Error modeling and path planning for freeform surfaces by laser triangulation on-machine measurement, IEEE Transactions on Instrumentation and Measurement 70 (2021) 1–11.
[12] R. Wang, A. Wu, X. Chen, J. Wang, A point and distance constraint based 6r robot calibration method through machine vision, Robotics and Computer-Integrated Manufacturing 65 (2020) 101959.
[13] J. He, L. Gu, G. Yang, Y. Feng, S. Chen, Z. Fang, A local poe-based self-calibration method using position and distance constraints for collaborative robots, Robotics and Computer-Integrated Manufacturing 86 (2024) 102685.
[14] A. Joubair, I. A. Bonev, Kinematic calibration of a six-axis serial robot using distance and sphere constraints, The International Journal of Advanced Manufacturing Technology 77 (1) (2015) 515–523.
[15] W. T. Estler, S. D. Phillips, B. Borchardt, T. Hopp, M. Levenson, K. Eberhardt, M. McClain, Y. Shen, X. Zhang, Practical aspects of touch-trigger probe error compensation, Precision Engineering 21 (1) (1997) 1–17.
[16] N. Wan, Q. Zhuang, Y. Guo, Z. C. Chen, Z. Fang, A new stylus orientation planning strategy for sculpture surface inspection based on touch position graph, Measurement 199 (2022) 111473.
[17] Y. Li, L. Zeng, K. Tang, S. Li, A dynamic pre-travel error prediction model for the kinematic touch trigger probe, Measurement 146 (2019) 689–704.
[18] Y. Bai, D. Wang, Improve the robot calibration accuracy using a dynamic online fuzzy error mapping system, IEEE Transactions on Systems, Man, and Cybernetics, Part B (Cybernetics) 34 (2) (2004) 1155–1160.
[19] Y. M. Zhao, Y. Lin, F. Xi, S. Guo, P. Ouyang, Switch-based sliding mode control for position-based visual servoing of robotic riveting system, Journal of Manufacturing Science and Engineering 139 (4) (2017) 041010.
[20] Y. M. Zhao, Y. Lin, F. Xi, S. Guo, Calibration-based iterative learning control for path tracking of industrial robots, IEEE Transactions on industrial electronics 62 (5) (2014) 2921–2929.
[21] A. Q. Md, K. Jha, S. Haneef, A. K. Sivaraman, K. F. Tee, A review on data-driven quality prediction in the production process with machine learning for industry 4.0, Processes 10 (10) (2022) 1966.
[22] W. Sun, B. Yao, N. Zeng, B. Chen, Y. He, X. Cao, W. He, An intelligent gear fault diagnosis methodology using a complex wavelet enhanced convolutional neural network, Materials 10 (7) (2017) 790.
[23] Y. Bai, Z. Sun, J. Deng, L. Li, J. Long, C. Li, Manufacturing quality prediction using intelligent learning approaches: A comparative study, Sustainability 10 (1) (2017) 85.
[24] B. Bhandari, G. Park, Non-contact surface roughness evaluation of milling surface using cnn-deep learning models, International Journal of Computer Integrated Manufacturing 37 (4) (2024) 423–437.
[25] M. Leco, T. McLeay, V. Kadirkamanathan, A two-step machining and active learning approach for right-first-time robotic countersinking through in-process error compensation and prediction of depth of cuts, Robotics and Computer-Integrated Manufacturing 77 (2022) 102345.
[26] M. Leco, V. Kadirkamanathan, A perturbation signal based data-driven gaussian process regression model for in-process part quality prediction in robotic countersinking operations, Robotics and Computer-Integrated Manufacturing 71 (2021) 102105.
[27] B. Iñigo, A. Ibabe, G. Aguirre, H. Urreta, L. N. López de Lacalle, Analysis of laser tracker-based volumetric error mapping strategies for large machine tools, Metals 9 (7) (2019) 757.
[28] H.-W. Chiu, C.-H. Lee, Prediction of machining accuracy and surface quality for cnc machine tools using data driven approach, Advances in Engineering Software 114 (2017) 246–257.
[29] N. Tounsi, A. Otho, Identification of machine–tool–workpiece system dynamics, International Journal of Machine Tools and Manufacture 40 (9) (2000) 1367–1384.
[30] S. Ghafarizadeh, G. Lebrun, J.-F. Chatelain, Experimental investigation of the cutting temperature and surface quality during milling of unidirectional carbon fiber reinforced plastic, Journal of Composite Materials 50 (8) (2016) 1059–1071.
[31] M. Bozdemir, Prediction of surface roughness considering cutting parameters and humidity condition in end milling of polyamide materials, Computational intelligence and neuroscience 2018 (1) (2018) 5850432.
[32] S. Jozić, D. Bajić, L. Celent, Application of compressed cold air cooling: achieving multiple performance characteristics in end milling process, Journal of Cleaner Production 100 (2015) 325–332.
[33] X. Cerutti, K. Mocellin, S. Hassini, B. Blaysat, E. Duc, Methodology for aluminium part machining quality improvement considering mechanical properties and process conditions, CIRP Journal of Manufacturing Science and Technology 18 (2017) 18–38.

[34] X. Sourd, R. Zitoune, A. Hejjaji, M. Salem, A. Hor, D. Lamouche, Plain water jet cleaning of titanium alloy after abrasive water jet milling: Surface contamination and quality analysis in the context of maintenance, Wear 477 (2021) 203833.
[35] M. Papananias, T. E. McLeay, O. Obajemu, M. Mahfouf, V. Kadirkamanathan, Inspection by exception: A new machine learning-based approach for multistage manufacturing, Applied Soft Computing 97 (2020) 106787.
[36] Y.-Y. Song, L. Ying, Decision tree methods: applications for classification and prediction, Shanghai archives of psychiatry 27 (2) (2015) 130.
[37] K. Gurney, An introduction to neural networks, CRC press, 2018.
[38] J. H. Friedman, Greedy function approximation: a gradient boosting machine, Annals of statistics (2001) 1189–1232.
[39] L. Breiman, Random forests, Machine learning 45 (2001) 5–32.
[40] L. E. Peterson, K-nearest neighbor, Scholarpedia 4 (2) (2009) 1883.
[41] T. Blu, P. Thévenaz, M. Unser, Linear interpolation revitalized, IEEE Transactions on Image Processing 13 (5) (2004) 710–719.
[42] F. Pedregosa, G. Varoquaux, A. Gramfort, V. Michel, B. Thirion, O. Grisel, M. Blondel, P. Prettenhofer, R. Weiss, V. Dubourg, et al., Scikit-learn: Machine learning in python, the Journal of machine Learning research 12 (2011) 2825–2830.
[43] B. Pang, E. Nijkamp, Y. N. Wu, Deep learning with tensorflow: A review, Journal of Educational and Behavioral Statistics 45 (2) (2020) 227–248.
[44] A. Gulli, S. Pal, Deep learning with Keras, Packt Publishing Ltd, 2017.
[45] D. P. Kingma, Adam: A method for stochastic optimization, arXiv preprint arXiv:1412.6980 (2014).
[46] P. Bourke, Cross correlation, Cross Correlation", Auto Correlation—2D Pattern Identification 596 (1996).
[47] W.-J. Lin, S.-H. Lo, H.-T. Young, C.-L. Hung, Evaluation of deep learning neural networks for surface roughness prediction using vibration signal analysis, Applied Sciences 9 (7) (2019) 1462.
[48] Z. Wang, D. Gao, Y. Lu, K. Deng, Z. Yuan, M. Huang, T. Jiang, A mutual cross-attention fusion network for surface roughness prediction in robotic machining process using internal and external signals, Journal of Manufacturing Systems 82 (2025) 284–300.